Lithium Ion Nanocarriers Self-Assembled from Amphiphiles with Aggregation-Induced Emission Activity

Rongrong Xue,[†] Yuchun Han,[‡] Yunlong Xiao,[†] Jianbin Huang,[†] Ben Zhong Tang,*[,§] and Yun Yan*[,†]

[†]Beijing National Laboratory for Molecular Sciences, State Key Laboratory for Structural Chemistry of Unstable and Stable Species, College of Chemistry and Molecular Engineering, Peking University, Chengfu Road 202, Beijing 100871, China

[‡]Institute of Chemistry, Chinese Academy of Sciences, Beijing 100190, China

[§]Department of Chemistry, Hong Kong Branch of Chinese National Engineering Research Center for Tissue Restoration and Reconstruction, Institute of Molecular Functional Materials, Institute for Advanced Study, State Key Laboratory of Neuroscience, Division of Biomedical Engineering and Division of Life Science, The Hong Kong University of Science and Technology, Clear Water Bay, Kowloon, Hong Kong 999077, China

S *Supporting Information*

ABSTRACT: Lithium salts are extensively used to treat diseases such as bipolar disorder or chronic reduction, but they often trigger undesirable side effects in patients due to the accumulation of lithium ions in peripheral organs. A conventional strategy for fabricating nanocarriers is not applicable to lithium ions because of their difficulty in binding firmly to molecules in water and easy leakage due to their small size and high water solubility. We report here the successful fabrication of lithium ion nanocarriers in water with an amphiphile containing two ethylene oxide tetramers attached to a hydrophobic core showing aggregation-induced light emission (AIE). The amphiphile self-assembles into fluorescent spherical aggregates in water. Lithium ions are loaded into the spherical aggregates by binding to the ethylene oxide tetramer. This nanocarrier can enter cells facilely via an endocytosis process and does not affect the cell viability at concentrations of up to 100 μM. Moreover, the self-imaging ability of the nanocarriers can be used to track the location of lithium-based drugs. We expect that this strategy of fabricating lithium nanocarriers will pave the way for reducing the practical doses of lithium salt that are used in clinical therapy.

KEYWORDS: *lithium ion, nanocarriers, amphiphile, self-assembly, AIE activity, self-imaging*
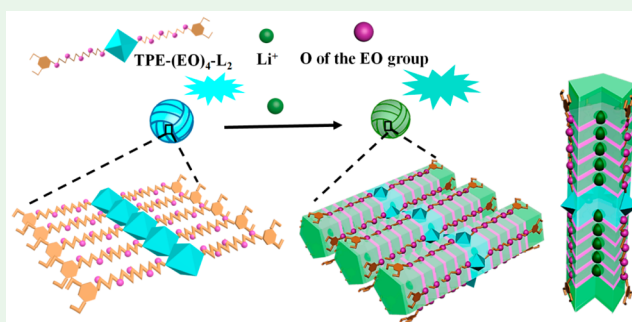
INTRODUCTION

Lithium salts, such as Li_2CO_3, LiCl, and LiI, are extensively used as effective drugs to treat bipolar disorder in patients, such as manic episodes and suicidality, and have been considered as possible drugs in the therapy of chronic neurodegenerative diseases, including Alzheimer's, Parkinson's, and Huntington's diseases.[1−5] However, the unnecessary accumulation of lithium ions in the kidney and heart can cause considerable side effects.[6,7] This is because lithium ions penetrate very slowly through the blood−brain barrier and across the biomembrane, so large doses are required for therapy to be effective.[8−10] To solve this problem, tremendous effort has been put into the search for alternatives to lithium. However, clinical outcomes have demonstrated that no alternatives have yet been able to show satisfactory bioactivities similar to lithium salts.[11−13] This is because the role of lithium in therapy is multifold and includes generating neuroprotective effects,[14−16] attenuating the production of inflammatory species,[17,18] and inhibiting the activity of certain enzymes.[19,20]

It is clearly challenging to obtain an alternative that can show all these abilities. Therefore, optimizing the performance of current lithium salts is probably the most practical strategy for a desirable therapy. To this goal, Adam J. Smith and co-workers[21,22] synthesized the first ionic cocrystals (ICCs) of lithium salts composed of organic anions. Although the resultant lithium ICCs indeed showed a more attractive in vivo pharmacokinetic performance, in vivo tests revealed considerable side effects.

Because the side effects of lithium therapy are caused by the accumulation of excess lithium ions in organs due to their slow penetration through the blood−brain barrier and across the cell membrane, it is easy to suggest the idea of loading lithium salts with nanocarriers, which can enter cells readily through endocytosis. However, progress in this aspect has lagged far
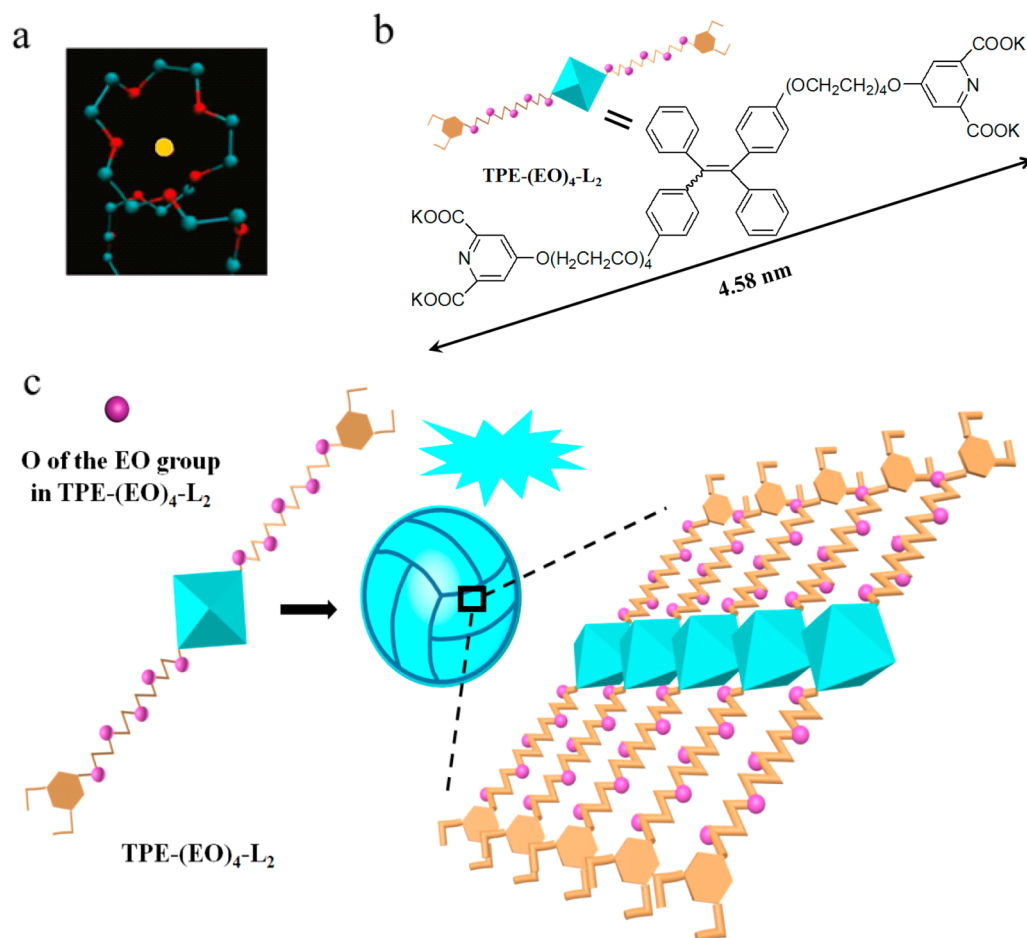
Scheme 1[a]

[a](a) Illustration of the binding mode for a Li⁺ with a long PEO chain.[34] (b) The molecular structure of TPE-(EO)$_4$-L$_2$. (c) The self-assembly of TPE-(EO)$_4$-L$_2$.

behind the development of nanocarriers for other drugs, mainly due to the challenge in fabricating proper nanocarriers for lithium ions. The lithium ion is very small, and lithium salts are highly soluble in water, which results in easy leaking of the ion. It is well-known that lithium ions can bind to crown ethers via a host–guest interaction[23–25] but that the crown ethers cannot be used as biological carriers due to their strong toxicity. To date, few successful cases for the loading of lithium ions have been reported; exceptional examples include the fabrication of a hexafunctional lipophilic envelope based on the synthesis of a series of lipophilic molecules[26] and a low-dose lithium microemulsion based on Peceol and lecithin.[27] In both cases, organic solvent is required. Therefore, developing lithium nanocarriers for use in an aqueous system remains a great challenge.

The key to fabricating aqueous lithium nanocarriers is to enhance the binding ability of lithium ions to the nanocarriers in water. It is well-known that poly(ethylene oxide) (PEO) can coordinate with lithium ions with high stability,[28–30] which is widely utilized in the fabrication of lithium batteries.[31,32] Previous experiments have verified that ∼4−5 EO units may bind with one Li⁺ to form a pseudo crown-ether structure[33,34] (Scheme 1a). This inspires, under the proper conditions, the use of EO groups in the fabrication of nanocarriers for Li⁺ might be possible. However, to date, no literature in this regard has appeared

Herein, we report that by using an EO-containing amphiphile TPE-(EO)$_4$-L$_2$ (Scheme 1b; TPE = tetraphenylethelene), we can obtain a lithium nanocarrier in water. TPE-(EO)$_4$-L$_2$ is designed to carry two (EO)$_4$ groups attached to a hydrophobic TPE core. The four EO units are supposed to bind to one Li⁺, and the TPE group is used as a reporter to check the formation of the nanocarrier and its penetration status through the cell membrane. This is because the propeller-shaped TPE core can show aggregation-induced light emission (AIE).[35–39] Since the (EO)$_4$ groups are water-soluble, the TPE-(EO)$_4$-L$_2$ aggregates in water above a critical concentration, which is accompanied by a significant increase in fluorescence. The binding of Li⁺ readily occurs in aggregates of TPE-(EO)$_4$-L$_2$, which can further enhance the fluorescence and increase the zeta potential of the TPE-(EO)$_4$-L$_2$ aggregates. The lithium ions that are loaded in the nanocarrier formed with TPE-(EO)$_4$-L$_2$ can penetrate through the cell membrane via the endocytosis process, which can be visualized by the fluorescence of the TPE moiety. Moreover, the TPE-(EO)$_4$-L$_2$ nanocarriers show satisfactory biocompatibility. To the best of our knowledge, this is the first demonstration of a lithium ion nanocarrier made in water that shows a self-imaging capability. We expect that applying this principle of constructing lithium ion nanocarriers will significantly reduce the side effects associated with lithium therapy and open a new
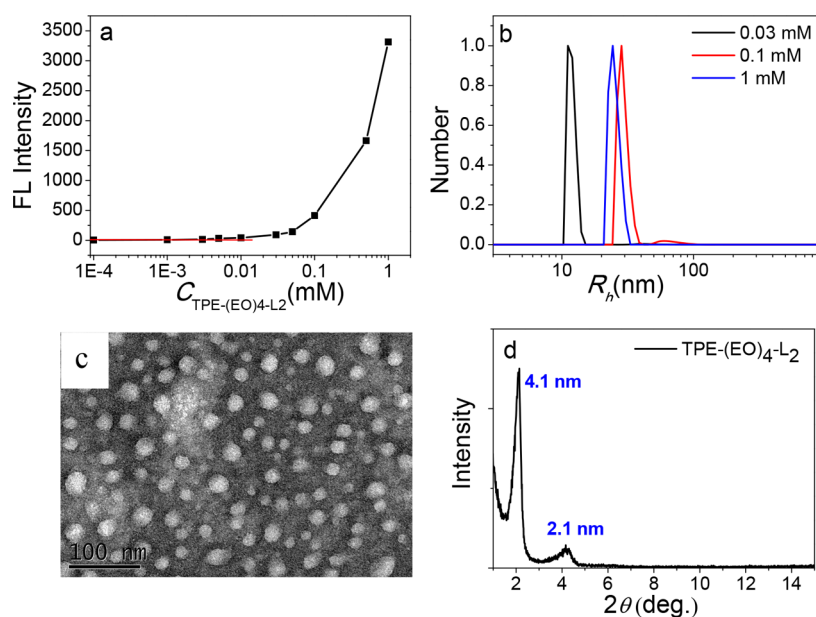
Figure 1. (a) Plot of fluorescence intensity against concentration of TPE-$(EO)_4$-L_2. (λ_{ex}: 365 nm; λ_{em}: 480 nm); (b) DLS data for TPE-$(EO)_4$-L_2 solution measured at different concentrations (average hydrodynamic radiis are concentration-dependent: 0.03 mM: 11 ± 2 nm; 0.1 mM: 28 ± 3 nm; 1 mM: 24 ± 5 nm); (c) TEM image of particles formed in 0.1 mM TPE-$(EO)_4$-L_2 solution; (d) XRD patterns of the spherical aggregates.

route toward treating diseases relating to bipolar disorder or chronic reduction.

RESULTS AND DISCUSSION

1. Self-Assembly Behavior of TPE-$(EO)_4$-L_2. TPE-$(EO)_4$-L_2 was synthesized in our lab (Scheme 1b).[40] Because of the presence of hydrophilic pyridine-2, 6-dicarboxylic acid and ethylene oxide tetramer moieties, this molecule forms clear solution in water. However, aggregation occurs as the concentration reaches to a critical value. Because of the aggregation-induced emission of the TPE group,[35−39] we determined the critical aggregation concentration (CAC) of TPE-$(EO)_4$-L_2 by monitoring the change in fluorescence intensity with increasing concentration of TPE-$(EO)_4$-L_2 ($C_{TPE-(EO)4-L2}$). In Figure 1a, we show that a sharp kink occurs at 0.01 mM, indicating the CAC for TPE-$(EO)_4$-L_2 is ∼0.01 mM. Dynamic light scattering (DLS) measurements (Figure 1b) show the presence of particles with average hydrodynamic radii depending on $C_{TPE-(EO)4-L2}$. TEM observations (Figure 1c and Figure S1) show that these particles are spherical aggregates.

X-ray diffraction (XRD) shows two diffraction peaks (Figure 1d) at $2\theta = 2.1°$ and $4.2°$, corresponding to $d_{001} = 4.1$ nm and $d_{002} = 2.1$ nm, respectively, suggesting the presence of a lamellar structure in the particles. The distance of 4.1 nm is very close to the fully extended length of the TPE-$(EO)_4$-L_2 (4.6 nm, see in Scheme 1b), indicating that the particles are probably formed by TPE-$(EO)_4$-L_2 molecules arranged layer-by-layer. The layer thickness can be obtained from atomic force microscopy (AFM) measurements of the height of dried particles, which reflects the fundamental layer thickness of the particle. Figure S2 reveals the different heights measured for the dried particles, including 8, 12, 16, 20, 24, and 28 nm. These heights are ∼2, 3, 4, 5, 6, and 7 times the extended length of TPE-$(EO)_4$-L_2, which suggests that the particles are solid, because the thickness of a hollow vesicle membrane is always equivalent to an even number of times the extended

length of TPE-$(EO)_4$-L_2. On the basis of this information, the molecular arrangement in the spherical TPE-$(EO)_4$-L_2 aggregates is illustrated in Scheme 1c.

The solid spherical particles remain stable in the phosphate-buffered saline (PBS) buffer or at biological salt concentration (Figure S3a,b), but their size decreases in the presence of 150 mM of salt (Figure S4). This is due to the shieling effect of the anionic charges on the head of TPE-$(EO)_4$-L_2. Therefore, the reduced repulsive force between the TPE-$(EO)_4$-L_2 molecules leads to reduction in the size of the particles. This also explains the reduction in particle size in Figure 1b, because any increase in the concentration of TPE-$(EO)_4$-L_2 may also raise the concentration of the counterions. Nevertheless, the sizes of all the spherical particles are much smaller than 100 nm, indicating that they can penetrate the blood−body barriers (BBB) system in the case of practical application.[41−43] Moreover, the fluorescence of the particles increases with increasing salt concentration (Figure S5a,b), suggesting that the shielding of the charges on the TPE-$(EO)_4$-L_2 molecule promotes the AIE effect.

2. Construction of Fluorescent Nanocarriers for Li⁺. *2.1. Formation of the Nanocarriers for Li⁺.* Since there is an abundance of EO groups in the nanoparticles formed by TPE-$(EO)_4$-L_2, we expect the strong binding of EO to lithium to enable the loading of lithium ions. Indeed, the negative zeta-potential of the TPE-$(EO)_4$-L_2 nanoparticles (Table 1) is reduced upon the addition of Li⁺ to TPE-$(EO)_4$-L_2 solution, and it becomes nearly zero at Li⁺/TPE-$(EO)_4$-L_2 = 6, indicating the successful binding of positive Li⁺ to negatively charged TPE-$(EO)_4$-L_2 nanoparticles. Consistent with the

Table 1. Variation of Zeta Potential Following Addition of Li_2CO_3

composition of the solution	zeta potential (mV)
TPE-$(EO)_4$-L_2 1 mM	−16.4 ± 1.0
TPE-$(EO)_4$-L_2/Li⁺ 1 mM/6 mM	−0.5 ± 1.5

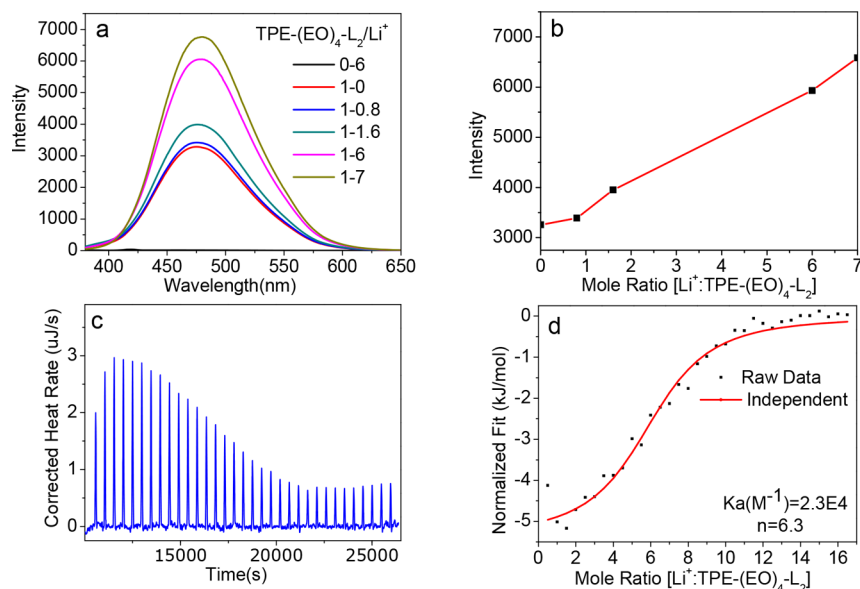**Figure 2.** Variation of fluorescence intensity with increasing molar ratio of $Li^+/TPE-(EO)_4-L_2$ (a, b); ITC titration data (c) and fitting curves (d) for Li^+ titrated into $TPE-(EO)_4-L_2$.

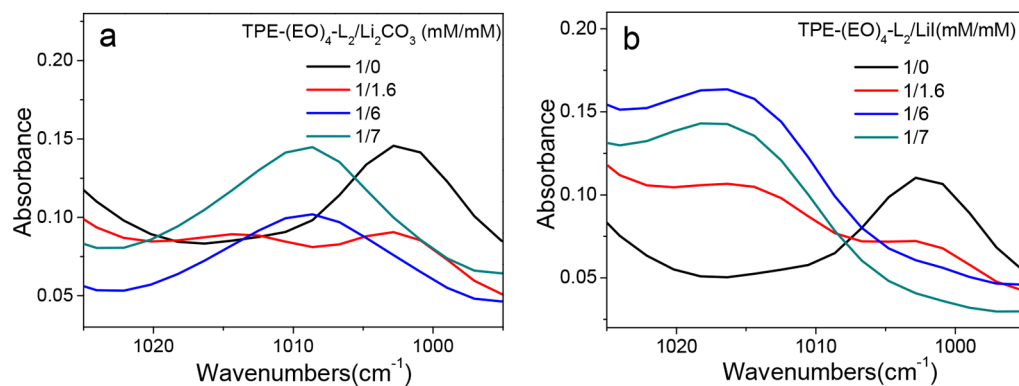**Figure 3.** Variation of IR spectra upon addition of Li_2CO_3 (a) or LiI (b) to 1 mM $TPE-(EO)_4-L_2$. The numbers in the figures are the concentration (molar) ratios between $TPE-(EO)_4-L_2$ and the lithium salts.

binding of Li^+ to the nanoparticles, the fluorescence intensity increases with increasing molar ratio of $Li^+/TPE-(EO)_4-L_2$ (Figure 2a,b), suggesting the enhanced aggregation of $TPE-(EO)_4-L_2$ due to the reduced electronic repulsion inside the $Li^+/TPE-(EO)_4-L_2$ nanoparticles.

The binding of Li^+ with $TPE-(EO)_4-L_2$ was further confirmed by isothermal titration calorimetry (ITC) measurements (Figure 2c,d). Exothermal peaks were observed upon the addition of lithium salt to the aqueous solution of $TPE-(EO)_4-L_2$, with the binding ratio determined to be $Li^+/TPE-(EO)_4-L_2 = 6$. The binding constant K_a is $\sim 2.3 \times 10^4$ M^{-1}, which is of the same order as the reported host–guest binding between cyclodextrins and surfactants.[44−47]

2.2. Driving Force for the Construction of Nanocarriers for Li^+. To determine the binding position of Li^+ in the $TPE-(EO)_4-L_2$ molecule, Fourier transform infrared (FT-IR) measurements were performed (Figure 3). The data show that the vibration of the $O-CH_2$ group is shifted to a larger wavenumber following the addition of various lithium salts into $TPE-(EO)_4-L_2$ solution. For instance, the wavenumber changes from 1002 to 1009 cm^{-1} for the $TPE-(EO)_4-L_2/$ Li_2CO_3 system and from 1002 to 1017 cm^{-1} for the $TPE-(EO)_4-L_2/LiI$ system, suggesting the binding of O to Li^+. In

addition, the vibration of the COO^- group of $TPE-(EO)_4-L_2$ is influenced by the added Li^+ (see Figure S6), indicating binding of Li^+ to the COO^- groups, too. Recalling the binding ratio of $Li^+/TPE-(EO)_4-L_2 = 6$ obtained from ITC measurements, we can postulate that all four COO^- groups are bound with Li^+ ions, with one Li^+ per COO^-. Clearly, the other two Li^+ ions are bound to the two $(EO)_4$ groups. This means that on average each $(EO)_4$ chain, which contains five O atoms, binds with one Li^+ ion. This is in perfect agreement with the theoretical binding number of O to Li^+ obtained in lithium salt-PEO systems.[33]

It is worth noting that the binding of Li^+ does not considerably affect the aggregation behavior of $TPE-(EO)_4-L_2$ and that the stability of the particles remains unchanged. Figure 4a shows that the CAC of $TPE-(EO)_4-L_2$ is nearly the same before and after the addition of Li^+. TEM observation confirms that the aggregates are still spherical particles, but DLS measurements indicate a slight decrease in size (Figure 4b), which is within our expectations: since the binding of Li^+ reduces the zeta potential of the particles to ~ 0, the repulsive forces inside the particles decrease, which should result in a shrinking of the particle size. Moreover, the small size endows
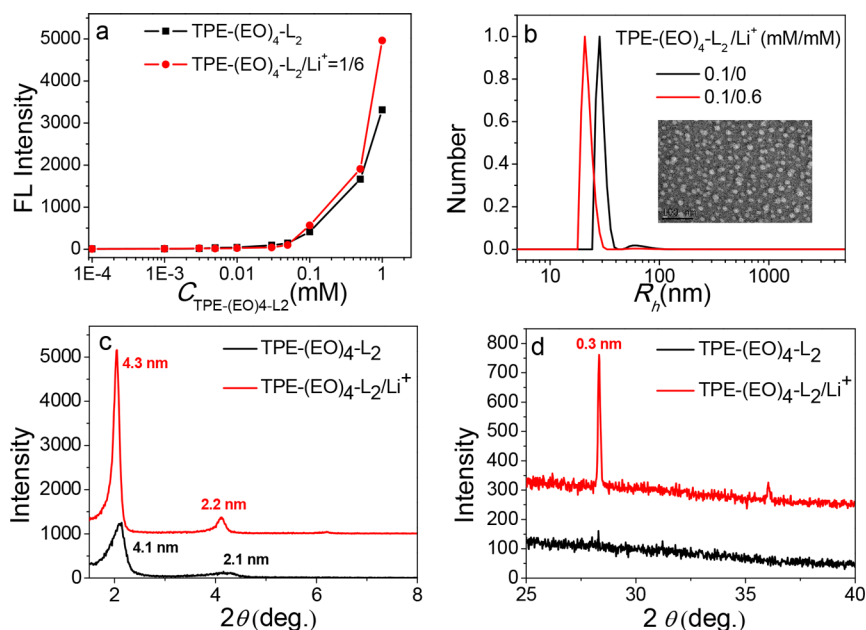
Figure 4. (a) The change in PL intensity with increasing $C_{TPE-(EO)4-L2}$ with and without Li^+. (b) The change in the particle size distribution upon addition of Li^+. (inset) TEM image for 0.1 mM TPE-$(EO)_4$-L_2 /Li^+ (d = 16 ± 3 nm). (c, d) XRD patterns of the TPE-$(EO)_4$-L_2/ Li^+ system in low- and wide-angle regions, respectively.

particles with stronger thermal motion, which prevents the further accumulation of the particles.

However, the XRD measurement suggests that the TPE-$(EO)_4$-L_2 molecules take on a much more stretched conformation in the lamellar packing. Figure 4c shows the presence of two diffraction peaks with corresponding d values of 4.3 and 2.2 nm. Clearly, the distance between the 001 diffraction planes for the Li^+/TPE-$(EO)_4$-L_2 system is larger than that for the TPE-$(EO)_4$-L_2 system, which is 4.1 nm. Therefore, the five O atoms in the one $(EO)_4$ moiety do not bind with one Li^+ in the same way as they do in a crown ether or PEO chains that show a bending effect (Scheme 1a). It is possible that one Li^+ (green sphere) binds with the five O (pink spheres) from five TPE-$(EO)_4$-L_2 molecules aligned in parallel, as indicated by the pentagonal prism in Scheme 2a. Since each TPE-$(EO)_4$-L_2 contains 10 O atoms, the five parallel TPE-$(EO)_4$-L_2 molecules can bind 10 Li^+ altogether, with the Li^+ ions aligned in a straight line (Scheme 2b,c). This conformation generates electrostatic repulsion between the Li^+ ions, so the TPE-$(EO)_4$-L_2 molecules in the solid sphere (Scheme 2d) take on a more extended conformation, as observed in the XRD measurements.

Interestingly, a sharp peak corresponding to a distance of 0.3 nm is observed in the XRD pattern for the Li^+/TPE-$(EO)_4$-L_2 system (Figure 4d). This peak is very distinct and is found in all measurements for the Li^+/TPE-$(EO)_4$-L_2 system, but it is never present in the absence of Li^+. Therefore, we contribute it to the array of Li^+ in the pentagonal prism. On the basis of this model, the extended length of the TPE-$(EO)_4$-L_2 can be estimated by summing the length of the TPE moiety, pyridine-dicarboxylate group, and Li^+ array, which gives a value of ∼4.4 nm. This is in good agreement with the distance of 4.3 nm obtained from the XRD measurements, verifying the rationality of our postulation.

We postulate the rigidity of the short $(EO)_4$ group may be responsible for such a coordinating mode. Indeed, quantum chemistry calculation (Figure S7) indicates that the TPE-

$(EO)_4$-L_2 molecule does not bend when two Li^+ ions are added, which is in perfect agreement with the experimental results. Moreover, the AFM measurements in Figure S8 reveal that the height of the particles is similar to that for the TPE-$(EO)_4$-L_2 systems, thus confirming the extended conformation of the TPE-$(EO)_4$-L_2 molecules in the particles. However, it is the stacking of the randomly oriented TPE-$(EO)_4$-L_2 /Li^+ cylinders that finally generates the solid spherical particles, as illustrated in Scheme 2d.

The special molecular structure of TPE-$(EO)_4$-L_2 is very crucial for the successful binding of lithium ions. Although PEO is well-known for its ability to bind with lithium ions, such a scenario does not occur in dilute water solution. If we replace the elegant structure of TPE-$(EO)_4$-L_2 with an L_2EO_4 (see the molecular structure in Figure S9) molecule that shows excellent water solubility and does not aggregate,[48−53] no binding of Li^+ occurs (Figure S6e and Table S1). Similarly, lithium binding does not occur if the PEO block exists as a protective corona shell outside a micellar structure (Figure S10). We expect that sufficient dehydration of PEO is crucial for the lithium binding. Indeed, in the lithium ion battery industry, PEO is processed as a polymer melt when binding with lithium ions.[31,32] In the present study, the local concentration of the EO groups in the particles is extremely high, which is similar to the environment of a polymer melt formed by PEO. Therefore, the binding of Li^+ to the EO groups occurs via aggregates formed with TPE-$(EO)_4$-L_2.

2.3. Release of Li+ from the Nanoparticles under Biological Conditions. Because the stability of the TPE-$(EO)_4$-L_2/ Li^+ nanoparticles under biological conditions is very relevant to their application, the binding status of Li^+ in 150 mM NaCl and PBS buffer was studied. ITC titration measurements (Figure 5a) indicate that the binding ratio is lowered to 2 in 150 mM NaCl, indicating that ∼67% of the Li^+ ions can be released from the nanoparticles. Therefore, the Li^+ ions bound to the COO^- group can be facilely released under biological conditions, whereas the EO-Li^+ coordination

Scheme 2. Illustration for the Binding of Li$^+$ (green sphere) to TPE-(EO)$_4$-L$_2$ Molecules[a]
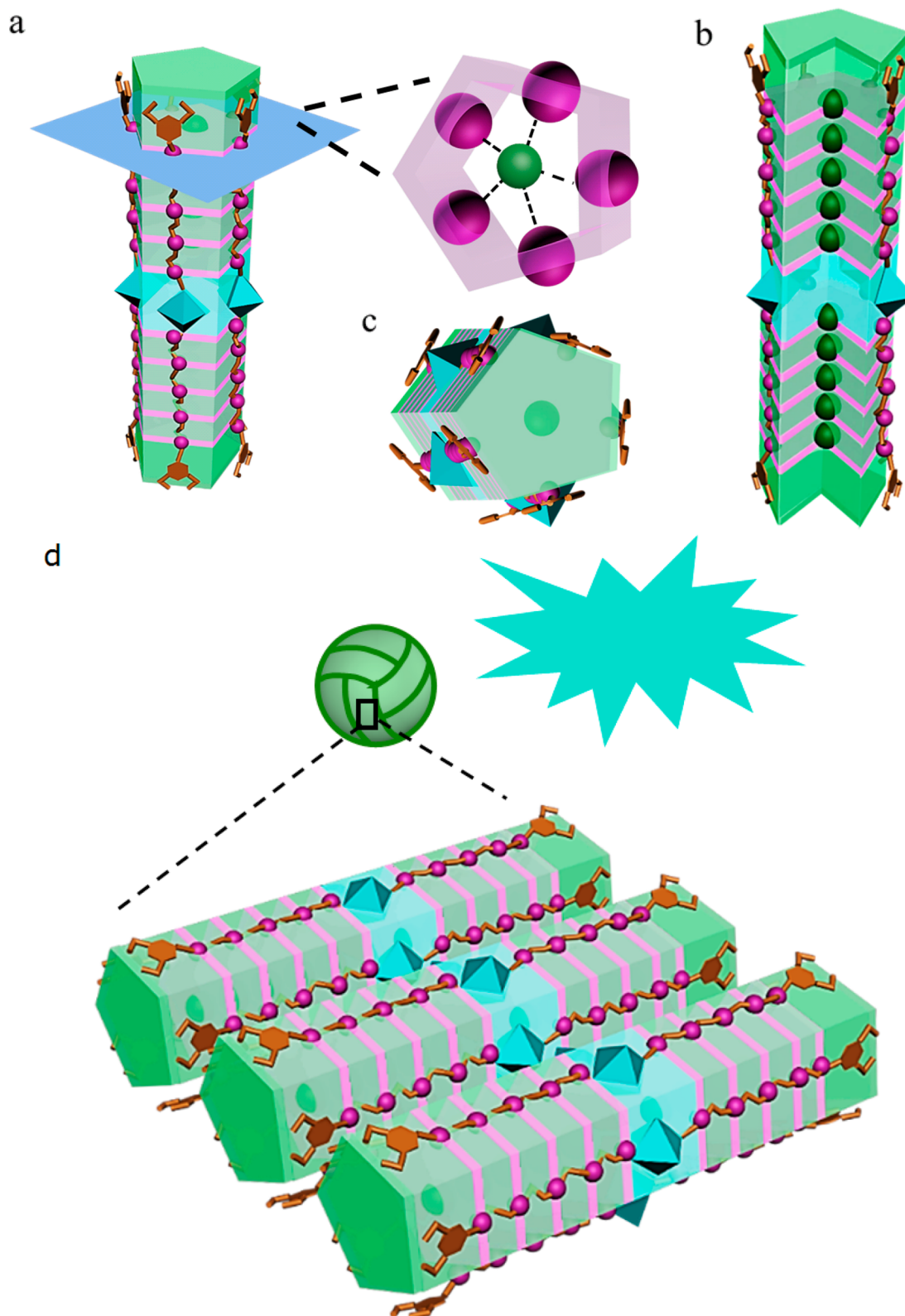
[a]One Li$^+$ (green sphere) binds with five O (pink spheres) from five TPE-(EO)$_4$-L$_2$ molecules aligned in parallel, as indicated by the pentagonal prism (a). Since each TPE-(EO)$_4$-L$_2$ contains 10 O atoms, the five parallel aligned TPE-(EO)$_4$-L$_2$ molecules can bind 10 Li$^+$ altogether, with the Li$^+$ ions probably aligned in a straight line, as shown in Scheme 2b,c. The stacking of the pentagonal prisms formed with TPE-(EO)$_4$-L$_2$/Li$^+$ into solid spheres (d).

interaction remains very stable, but it is not clear whether this fraction of Li$^+$ ions can be sufficiently utilized in vitro. The

weaker binding of Li$^+$ ions bound to the COO$^-$ group suggests that interaction between them mainly involves electrostatic
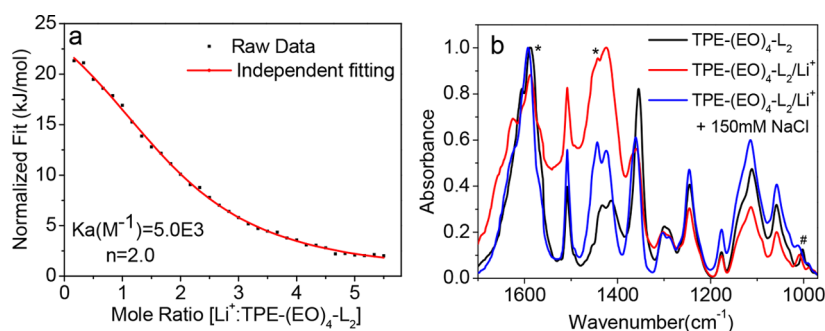
Figure 5. (a) ITC titration data and fitting curves for Li^+ titrated into TPE-$(EO)_4$-L_2 with [NaCl] = 150 mM. (b) Variation of FT-IR spectra for TPE-$(EO)_4$-L_2/Li^+ solution with or without NaCl (#) EO group:1000−1300 cm^{-1}; (*) COO^-: asymmetrical stretching vibration: 1650−1550 cm^{-1}, symmetric stretching vibration: ~1400 cm^{-1}).
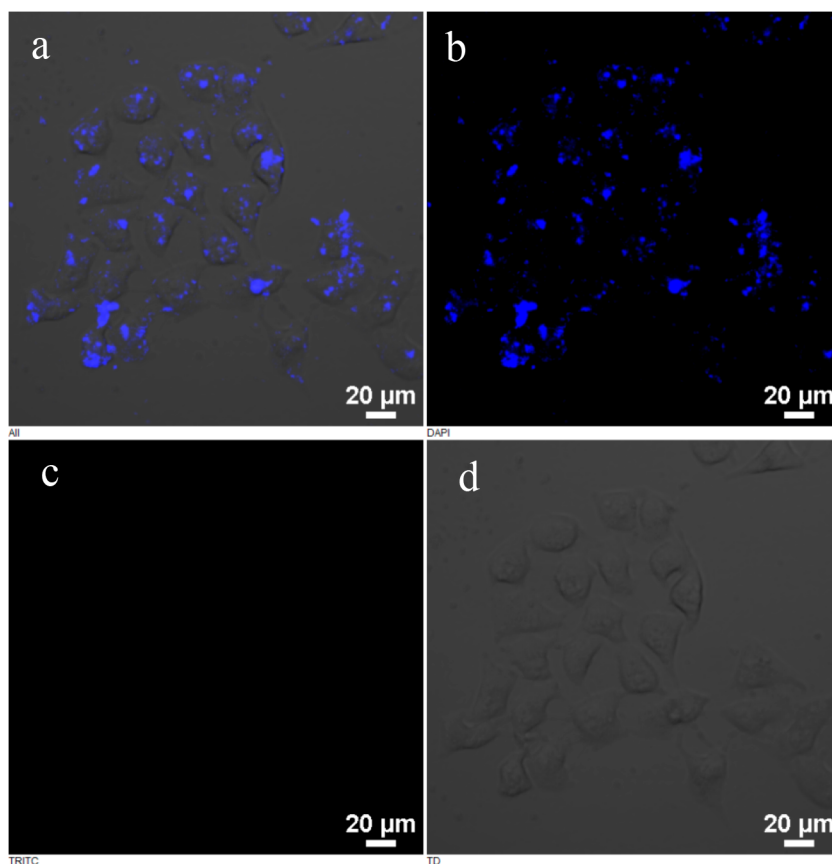

Figure 6. Confocal fluorescence images of living HeLa cells incubated for 12 h with solutions of TPE-$(EO)_4$-L_2/Li^+(1/6) ([TPE-$(EO)_4$-L_2] = 0.1 mM) (a) overlap of (b−d), which are images obtained at detector slit 425−475 nm (b), detector slit 552−617 nm (c), and bright field (d), respectively.

forces, which can be shielded in a saline environment. This is further confirmed by FT-IR measurements (Figure 5b), where a larger wavenumber for the vibration of the O−CH_2 bonds is observed (with 150 mM NaCl: wavenumber changes from 1002 to 1013 cm^{-1}; without 150 mM NaCl: wavenumber changes from 1002 to 1009 cm^{-1}), whereas the vibration of COO^- groups shows a recovery (partially magnified spectra in Figure S11). As in the TPE-$(EO)_4$-L_2 system, DLS and TEM measurements (Figure S12) confirm the presence of spherical particles under these conditions, thus verifying robust stability in a biological environment. Therefore, the nanocarriers are expected to show potential for use in in vitro application.

3. Application of the Fluorescent Nanocarriers for Li^+. So far, we constructed the nanocarriers for Li^+ based on TPE-$(EO)_4$-L_2, which is a self-fluorescent spherical nanoparticle with small size, zero surface charge, and excellent stability. Next, we study its biocompatibility and imaging ability in cells. The cell experiment clearly indicates that these nanoparticles can be taken up by HeLa cells and hRPE cells. No blue emission can be observed after the HeLa cells were incubated for 12 h in deionized water or Li^+ solution (Figure S13). However, strong blue emission is observed after the HeLa cells were incubated in a solution of TPE-$(EO)_4$-L_2/Li^+ for 12 h (Figure 6). Moreover, the cytotoxicity of these nanoparticles is negligible to HeLa cells (Figure 7). Similar imaging ability and cytotoxicity is observed for hRPE cells (Figures S14−S16), but a longer incubation time of 24 h is required.
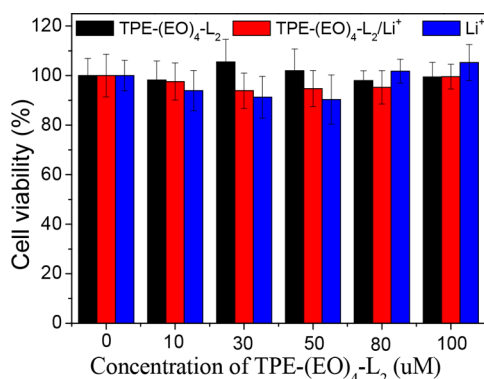
Figure 7. Viability of HeLa cells treated with different concentrations of the nanocarriers with or without Li^+ and Li_2CO_3 solutions.

CONCLUSION

We have designed an amphiphile TPE-$(EO)_4$-L_2 molecule that contains EO and TPE groups and can self-assemble into spherical aggregates. Lithium ions can bind to the EO groups inside the aggregates, which enables the realization of self-fluorescence labeled nanocarriers for lithium ions. This type of nanocarrier, with its small size, retains a fluorescent property and demonstrates good biocompatibility. We expect the lithium nanocarriers to be applied in the clinical treatment of mental illness and pave the way for creating a new generation of lithium-based drugs.

EXPERIMENTAL SECTION

Materials. *Synthesis of the Amphiphilic AIE Fluorogen TPE-$(EO)_4$-L_2.* TPE-$(EO)_4$-L_2(L: dicaboxypyridine group) used in this work was synthesized following previously reported procedures.[40]

Other Materials. The other chemicals were obtained from Beijing Chemical Reagents Co. and were all of A.R. grade. Distilled water was purified through a Milli-Q Advantage A10 ultrapure water system.

Sample Preparation. The solutions were obtained by dissolving the solid TPE-$(EO)_4$-L_2 or soluble lithium salts in ultrapure water.

The solutions of TPE-$(EO)_4$-L_2/Li^+ were obtained by mixing simply TPE-$(EO)_4$-L_2 solution and Li^+ solution at the desired concentration. The final concentration of TPE-$(EO)_4$-L_2 and Li^+ was controlled at [TPE-$(EO)_4$-L_2]/[Li^+] = 1/6. All experiments were performed at room temperature (~25 °C).

Methods. *Transmission Electron Microscopy.* An FEI Tecnai G2 T20 TEM was used to observe the morphology of the aggregates. Samples were placed onto 230 mesh copper grids coated with Formvar film. Excess water was removed with filter paper. Then, a drop of uranyl acetate (0.5%, in ethanol) solution was added to the film for 30 s for negative staining. Excess staining liquid was removed similar to the previous operation. Finally, samples were dried in ambient air at room temperature before TEM observation.

Fluorescence Spectrometer Measurements. Steady-state fluorescence spectra were obtained with a Hitachi F-7000 fluorescence spectrometer. The excitation and emission wavelengths were set at 365 and 480 nm, respectively. Other conditions: slit, 5 mm; scanning speed: 240 nm/min; photomultiplier tube (PMT) voltage: 700 V.

Dynamic Light Scattering. DLS measurements were performed using an ALV/DLS/SLS-5022F light-scattering apparatus. The incident beam wavelength was 632.8 nm, generated from a 22 mW He–Ne laser. Measurements were conducted at ambient temperature. The solutions were processed to be dust-free using a 0.45 μm hydrophilic polyvinylidene (PVDF) membrane before measurements. The scattering angle was set at 90°, and the intensity auto correlation functions were analyzed by the CONTIN method.[54,55]

Atomic Force Microscopy. AFM measurements were conducted using a D3100 AFM (VEECO, USA) setup. One drop of sample solution was spin-coated onto a mica surface, which was then observed by AFM under tapping mode.

Attenuated Total Reflection Infrared. A Nicolet iN10 MX microscopic infrared spectrometer equipped with an attenuated total reflection (ATR) accessory (Thermo Scientific Co., USA) was utilized to conduct the IR measurements. Sample solutions were drop cast onto a CaF_2 plate and allowed to dry under ambient conditions. Then, the IR spectra of the sample solutions were collected in the range from 4000 to 650 cm^{-1}. Each measurement was averaged on the basis of 32 scans, with a resolution of 4 cm^{-1}.

X Ray Diffraction. Reflection XRD studies were performed using a model XKS-2000 X-ray diffractometer (Scintaginc). The X-ray wavelength was obtained from a Cu Kα1 beam (λ = 1.5406 Å) generated with a Cu anode. Samples were prepared by drop casting solution onto a clean glass slide before being placed in a drier for over 24 h. Low-angle and wide-angle measurements were conducted separately in the 2θ ranges of 0.6−15° and 3−50°, respectively.

Isothermal Titration Calorimetry (ITC). ITC measurements were performed in a TAM 2277−201 microcalorimetric system (Thermometric AB, Järfälla, Sweden) at 298.15 ± 0.01 K. A stainless steel syringe with a volume of 1 mL was used in all the experiments. The sample cell was initially loaded with 0.6 mL of water or TPE-$(EO)_4$-L_2 solution. Then, solutions containing Li^+ were injected into the sample cell via a 500 μL Hamilton syringe. A series of injections was performed all controlled by a 612 Thermometric Lund pump. After each injection, the system was stirred at 60 rotations per minute with a gold propeller to ensure sufficient mixing. Heat flow against time was recorded for each injection. The enthalpy (ΔH_{obs}) was obtained by integration over the peak observed in the plot of the heat flow. The dilution heats were subtracted from all the measurements. The binding stoichiometry n, binding constant (K), and binding enthalpy (DH) were obtained by fitting the observed enthalpy curves with the computer program TAM (Digitam 4.1 for Windows from Thermometric AB) and transforming each injection into the molar ratio of Li^+ to TPE-$(EO)_4$-L_2.

Theoretical Calculations. The Gaussian 09 package was used to calculate the molecular conformation of TPE-$(EO)_4$-L_2 before and after binding two Li^+ ions at restricted density functional theory level. The hybrid functional B3LYP and the 6-311+g (d, p) basis set were chosen for all the calculations. The initial locations of the Li^+ ions were set to be on the top of the oxygen and carbon atom, respectively, of the different EO groups. All calculations showed similar results, with a representative calculation outcome given in Supporting Information.

Confocal Fluorescent Images of Living Cell. A confocal laser scanning microscope (A1R-si, Nikon, Japan) was used to observe the living HeLa cells after incubation with the TPE-$(EO)_4$-L_2/Li^+ nanoparticles. The cells were imaged under fluorescence mode with a 60× immersion lens. Other experimental parameters: laser power of 100%, pinhole 2.0 AU, excitation wavelength of 405 nm, detector slit set at 425−475 nm, resolution of 1024 × 1024, and a scan speed of 0.5 frames/s.

Cell Culture. HeLa cell lines were cultured in a standard Dulbecco's modified Eagle's medium supplemented with 10% (v/v) fetal bovine serum, 100 U/mL of penicillin, and 100 μg/mL of streptomycin at 37 °C in a humidified incubator containing 5% CO_2 for 24 h. Cell growth was conducted by addition of the stock solution of TPE-$(EO)_4$-L_2/Li^+ to obtain a final TPE-$(EO)_4$-L_2 concentration of 0.1 mM for another 12 h in the dark at 37 °C.

Cytotoxicity Assay. A 3-(4,5-dimethylthiazol-2-yl)-2,5-diphenyltetrazolium bromide (MTT) assay[56] was used to measure the cell viability. HeLa cells (5×10^3) were seeded into a 96-well plate per well. The cell was incubated overnight at 37 °C in an atmosphere containing 5% CO_2. Then, various doses of 0−100 μM solutions were transferred into the aforementioned medium and immediately incubated at 37 °C. Control experiments were conducted in a similar manner for the medium without cells or TPE-$(EO)_4$-L_2/Li^+. After 12 or 24 h of incubation, 10 μL of MTT solution (5 mg/mL in PBS) was added into each well. Then, 4 h later, 150 μL of dimethyl sulfoxide (DMSO) was added to dissolve the formazan precipitate. The cell

survival rate was quantified by the optical density obtained using a spectrophotometer (Multiskan MK3, Thermo Scientific, USA). Optical density (OD) was read at 490 nm followed by the subtraction of the background at 630 nm. Every experiment was repeated six times.

■ ASSOCIATED CONTENT

Ⓢ Supporting Information

The Supporting Information is available free of charge on the ACS Publications website at DOI: 10.1021/acsanm.7b00050.

AFM images of TPE-$(EO)_4$-L_2 and TPE-$(EO)_4$-L_2/Li^+ solutions, DLS data and fluorescence spectra of TPE-$(EO)_4$-L_2 solution with different salt concentration, IR spectra, quantum chemistry calculation result, confocal fluorescent images, cell viability data (PDF)

■ AUTHOR INFORMATION

Corresponding Authors
*E-mail: tangbenz@ust.hk. (B.-Z.T.)
*E-mail: yunyan@pku.edu.cn. (Y.Y.)
ORCID ⊕
Yuchun Han: 0000-0002-2928-2633
Ben Zhong Tang: 0000-0002-0293-964X
Yun Yan: 0000-0001-8759-3918
Notes
The authors declare no competing financial interest.

■ ACKNOWLEDGMENTS

■ REFERENCES

(1) Marmol, F. Lithium: Bipolar Disorder and Neurodegenerative Diseases Possible Cellular Mechanisms of the Therapeutic Effects of Lithium. Prog. Neuro-Psychopharmacol. *Prog. Neuro-Psychopharmacol. Biol. Psychiatry* **2008**, *32*, 1761−1771.

(2) Chiu, C.-T.; Chuang, D.-M. Molecular Actions and Therapeutic Potential of Lithium in Preclinical and Clinical Studies of CNS Disorders. *Pharmacol. Ther.* **2010**, *128*, 281−304.

(3) Chiu, C.-T.; Wang, Z.; Hunsberger, J. G.; Chuang, D.-M. Therapeutic Potential of Mood Stabilizers Lithium and Valproic Acid: Beyond Bipolar Disorder. *Pharmacol. Rev.* **2013**, *65*, 105−142.

(4) Diniz, B. S.; Machado-Vieira, R.; Forlenza, O. V. Lithium and Neuroprotection: Translational Evidence and Implications for the Treatment of Neuropsychiatric Disorders. Neuropsychiatr. *Dis. Treat.* **2013**, *9*, 493−500.

(5) Forlenza, O. V.; Aprahamian, I.; de Paula, V. J.; Hajek, T. Lithium, a Therapy for AD: Current Evidence from Clinical Trials of Neurodegenerative Disorders. *Curr. Alzheimer Res.* **2016**, *13*, 879−886.

(6) Oakley, P. W.; Whyte, I. M.; Carter, G. L. Lithium Toxicity: an Iatrogenic Problem in Susceptible Individuals. *Aust. N. Z. J. Psychiatry* **2001**, *35*, 833−840.

(7) McKnight, R. F.; Adida, M.; Budge, K.; Stockton, S.; Goodwin, G. M.; Geddes, J. R. Lithium Toxicity Profile: a Systematic Review and Meta-analysis. *Lancet* **2012**, *379*, 721−728.

(8) Davenport, V. D. Distribution of Parenterally Administered Lithium in Plasma, Brain and Muscle of Rats. *Am. J. Physiol.* **1950**, *163*, 633−641.

(9) Ebadi, M. S.; Simmons, V. J.; Hendrickson, M. J.; Lacy, P. S. Pharmacokinetics of Lithium and Its Regional Distribution in Rat Brain. *Eur. J. Pharmacol.* **1974**, *27*, 324−329.

(10) Schou, M. Pharmacology and Toxicology of Lithium. *Annu. Rev. Pharmacol. Toxicol.* **1976**, *16*, 231−243.

(11) Thies-Flechtner, K.; Müller-Oerlinghausen, B.; Seibert, W.; Walther, A.; Greil, W. Effect of Prophylactic Treatment on Suicide Risk in Patients with Major Affective Disorders. *Pharmacopsychiatry* **1996**, *29*, 103−107.

(12) Kilbane, E. J.; Gokbayrak, N. S.; Galynker, I.; Cohen, L.; Tross, S. A Review of Panic and Suicide in Bipolar Disorder: Does Comorbidity Increase Risk? *J. Affective Disord.* **2009**, *115*, 1−10.

(13) Singh, N.; Halliday, A. C.; Thomas, J. M.; Kuznetsova, O. V.; Baldwin, R.; Woon, E. C.; Aley, P. K.; Antoniadou, I.; Sharp, T.; Vasudevan, S. R.; Churchill, G. C. A Safe Lithium Mimetic for Bipolar Disorder. *Nat. Commun.* **2013**, *4*, 1332−1338.

(14) Fukumoto, T.; Morinobu, S.; Okamoto, Y.; Kagaya, A.; Yamawaki, S. Chronic Lithium Treatment Increases the Expression of Brain-Derived Neurotrophic Factor in the Rat Brain. *Psychopharmacology* **2001**, *158*, 100−106.

(15) Leyhe, T.; Eschweiler, G. W.; Stransky, E.; Gasser, T.; Annas, P.; Basun, H.; Laske, C. Increase of BDNF Serum Concentration in Lithium Treated Patients with Early Alzheimer's Disease. *J. Alzheimer's Dis.* **2009**, *16*, 649−656.

(16) Croce, N.; Mathe, A. A.; Gelfo, F.; Caltagirone, C.; Bernardini, S.; Angelucci, F. Effects of Lithium and Valproic Acid on BDNF Protein and Gene Expression in an in Vitro Human Neuron-like Model of Degeneration. *J. Psychopharmacol. (London, U. K.)* **2014**, *28*, 964−972.

(17) Yuskaitis, C. J.; Jope, R. S. Glycogen Synthase Kinase-3 Regulates Microglial Migration, Inflammation, and Inflammation-induced Neurotoxicity. *Cell. Signalling* **2009**, *21*, 264−273.

(18) Zakeri, M.; Afshari, K.; Gharedaghi, M. H.; Shahsiah, R.; Rahimian, R.; Maleki, F.; Dehpour, A. R.; Javidan, A. N. Lithium Protects Against Spinal Cord Injury in Rats: Role of Nitric Oxide. J. *Neurol. Surg. A Cent. Eur. Neurosurg.* **2014**, *75*, 427−433.

(19) Pollack, S. J.; Atack, J. R.; Knowles, M. R.; McAllister, G.; Ragan, C. I.; Baker, R.; Fletcher, S. R.; Iversen, L. L.; Broughton, H. B. Mechanism of Inositol Monophosphatase, the Putative Target of Lithium Therapy. *Proc. Natl. Acad. Sci. U. S. A.* **1994**, *91*, 5766−5770.

(20) Phiel, C. J.; Klein, P. S. Molecular Targets of Lithium Action. *Annu. Rev. Pharmacol. Toxicol.* **2001**, *41*, 789−813.

(21) Smith, A. J.; Kim, S.-H.; Duggirala, N. K.; Jin, J.; Wojtas, L.; Ehrhart, J.; Giunta, B.; Tan, J.; Zaworotko, M. J.; Shytle, R. D. Improving Lithium Therapeutics by Crystal Engineering of Novel Ionic Cocrystals. *Mol. Pharmaceutics* **2013**, *10*, 4728−4738.

(22) Duggirala, N. K.; Smith, A. J.; Wojtas, Ł.; Shytle, R. D.; Zaworotko, M. J. Physical Stability Enhancement and Pharmacokinetics of a Lithium Ionic Cocrystal with Glucose. *Cryst. Growth Des.* **2014**, *14*, 6135−6142.

(23) Anet, F. A. L.; Dale, J.; Daasvatn, K.; Kristiansen, P. O.; Krane, J.; Swahn, C.-G. The Conformation of 1,4,7,10-Tetraoxacyclododecane and its 1:1 Lithium Salt Complexes. *Acta Chem. Scand.* **1973**, *27*, 3395−3402.

(24) Gadzekpo, V. P. Y.; Christian, G. D. 1,4,7,10-Tetraoxacyclododecane(12-Crown-4) as Neutral Carrier for Lithium Ion in Lithium Ion Selective Electrode. *Anal. Lett.* **1983**, *16*, 1371−1380.

(25) Al-Rusaese, S.; Al-Kahtani, A. A.; El-Azhary, A. A. Experimental and Theoretical Study of the Vibrational Spectra of 12-Crown-4−Alkali Metal Cation Complexes. *J. Phys. Chem. A* **2006**, *110*, 8676−8687.

(26) Shanzer, A.; Samuel, D.; Kornstein, R. Lipophilic Lithium Ion Carriers. *J. Am. Chem. Soc.* **1983**, *105*, 3815−3818.

(27) Pouladi, M. A.; Brillaud, E.; Xie, Y.; Conforti, P.; Graham, R. K.; Ehrnhoefer, D. E.; Franciosi, S.; Zhang, W.; Poucheret, P.; Compte, E.; Maurel, J. C.; Zuccato, C.; Cattaneo, E.; Neri, C.; Hayden, M. R. NP03, a Novel Low-Dose Lithium Formulation, is Neuroprotective in the YAC128 Mouse Model of Huntington Disease. *Neurobiol. Dis.* **2012**, *48*, 282−289.

(28) Armand, M. B. Polymer Electrolytes. *Annu. Rev. Mater. Sci.* **1986**, *16*, 245−261.

(29) Frech, R.; Huang, W. Conformational Changes in Diethylene Glycol Dimethyl Ether and Poly(ethylene oxide) Induced by Lithium Ion Complexation. *Macromolecules* **1995**, *28*, 1246−1251.

(30) Adebahr, J.; Gavelin, P.; Jannasch, P.; Ostrovskii, D.; Wesslen, B.; Jacobsson, P. Cation Coordination in Ion-Conducting Gels Based on PEO-Grafted Polymers. *Solid State Ionics* **2000**, *135*, 149−154.

(31) Young, W.-S.; Albert, J. N. L.; Schantz, A. B.; Epps, T. H. Mixed-Salt Effects on the Ionic Conductivity of Lithium-Doped PEO-Containing Block Copolymers. *Macromolecules* **2011**, *44*, 8116−8123.

(32) Bouchet, R.; Phan, T. N. T.; Beaudoin, E.; Devaux, D.; Davidson, P.; Bertin, D.; Denoyel, R. Charge Transport in Nanostructured PS−PEO−PS Triblock Copolymer Electrolytes. *Macromolecules* **2014**, *47*, 2659−2665.

(33) Johansson, P.; Tegenfeldt, J.; Lindgren, J. Modelling Amorphous Lithium Salt−PEO Polymer Electrolytes: ab Initio Calculations of Lithium Ion−Tetra-, Penta- and Hexaglyme Complexes. *Polymer* **1999**, *40*, 4399−4406.

(34) Diddens, D.; Heuer, A.; Borodin, O. Understanding the Lithium Transport within a Rouse-Based Model for a PEO/LiTFSI Polymer Electrolyte. *Macromolecules* **2010**, *43*, 2028−2036.

(35) Luo, J.; Xie, Z.; Lam, J. W. Y.; Cheng, L.; Chen, H.; Qiu, C.; Kwok, H. S.; Zhan, X.; Liu, Y.; Zhu, D.; Tang, B. Z. Aggregation-Induced Emission of 1-Methyl-1,2,3,4,5-Pentaphenylsilole. *Chem. Commun.* **2001**, 1740−1741.

(36) Tong, H.; Hong, Y.; Dong, Y.; Haubler, M.; Lam, J. W. Y.; Li, Z.; Guo, Z.; Guo, Z.; Tang, B. Z. Fluorescent "Light-Up" Bioprobes Based on Tetraphenylethylene Derivatives with Aggregation-Induced Emission Characteristics. *Chem. Commun.* **2006**, 3705−3707.

(37) Zhou, Z.; Yan, X.; Saha, M. L.; Zhang, M.; Wang, M.; Li, X.; Stang, P. J. Immobilizing Tetraphenylethylene into Fused Metalla-cycles: Shape Effects on Fluorescence Emission. *J. Am. Chem. Soc.* **2016**, *138*, 13131−13134.

(38) Feng, G.; Wu, W.; Xu, S.; Liu, B. Far Red/Near-Infrared AIE Dots for Image-Guided Photodynamic Cancer Cell Ablation. *ACS Appl. Mater. Interfaces* **2016**, *8*, 21193−21200.

(39) Li, J.; Liu, K.; Han, Y.; Tang, B. Z.; Huang, J.; Yan, Y. Fabrication of Propeller-Shaped Supra-amphiphile for Construction of Enzyme-Responsive Fluorescent Vesicles. *ACS Appl. Mater. Interfaces* **2016**, *8*, 27987−27995.

(40) Xu, L.; Jiang, L.; Drechsler, M.; Sun, Y.; Liu, Z.; Huang, J.; Tang, B. Z.; Li, Z.; Cohen Stuart, M. A.; Yan, Y. Self-Assembly of Ultralong Polyion Nanoladders Facilitated by Ionic Recognition and Molecular Stiffness. *J. Am. Chem. Soc.* **2014**, *136*, 1942−1947.

(41) Chithrani, B. D.; Ghazani, A. A.; Chan, W. C. W. Determining the Size and Shape Dependence of Gold Nanoparticle Uptake into Mammalian Cells. *Nano Lett.* **2006**, *6*, 662−668.

(42) Lu, F.; Wu, S.-H.; Hung, Y.; Mou, C.-Y. Size Effect on Cell Uptake in Well-Suspended, Uniform Mesoporous Silica Nano-particles. *Small* **2009**, *5*, 1408−1413.

(43) Gao, J.-Q.; Lv, Q.; Li, L.-M.; Tang, X.-J.; Li, F.-Z.; Hu, Y.-L.; Han, M. Glioma Targeting and Blood−Brain Barrier Penetration by Dual-Targeting Doxorubincin Liposomes. *Biomaterials* **2013**, *34*, 5628−5639.

(44) Dorrego, A. B.; García-Río, L.; Hervés, P.; Leis, J. R.; Mejuto, J. C.; Pérez-Juste, J. Micellization versus Cyclodextrin−Surfactant Complexation. *Angew. Chem., Int. Ed.* **2000**, *39*, 2945−2948.

(45) Jiang, L.; Peng, Y.; Yan, Y.; Huang, J. Aqueous Self-Assembly of SDS@2β-CD Complexes: Lamellae and Vesicles. *Soft Matter* **2011**, *7*, 1726−1731.

(46) Zhou, C.; Cheng, X.; Zhao, Q.; Yan, Y.; Wang, J.; Huang, J. Self-Assembly of Nonionic Surfactant Tween 20@2β-CD Inclusion Complexes in Dilute Solution. *Langmuir* **2013**, *29*, 13175−13182.

(47) Martín, V. I.; Ostos, F. J.; Angulo, M.; Márquez, A. M.; López-Cornejo, P.; López-López, M.; Carmona, A. T.; Moyá, M. L. Host-Guest Interactions between Cyclodextrins and Surfactants with Functional Groups at the end of the Hydrophobic Tail. *J. Colloid Interface Sci.* **2017**, *491*, 336−348.

(48) Vermonden, T.; van der Gucht, J.; de Waard, P.; Marcelis, A. T. M.; Besseling, N. A. M.; Sudhölter, E. J. R.; Fleer, G. J.; Cohen Stuart, M. A. Water-Soluble Reversible Coordination Polymers: Chains and Rings. *Macromolecules* **2003**, *36*, 7035−7044.

(49) van der Burgh, S.; de Keizer, A.; Cohen Stuart, M. A. Complex Coacervation Core Micelles. Colloidal Stability and Aggregation Mechanism. *Langmuir* **2004**, *20*, 1073−1084.

(50) Yan, Y.; Besseling, N. A. M.; de Keizer, A.; Marcelis, A. T. M.; Drechsler, M.; Cohen Stuart, M. A. Hierarchical Self-Assembly in Solutions Containing Metal Ions, Ligand, and Diblock Copolymer. *Angew. Chem., Int. Ed.* **2007**, *46*, 1807−1809.

(51) Yan, Y.; Besseling; de Keizer, A.; Drechsler, M.; Fokkink, R.; Cohen Stuart, M. A. Wormlike Aggregates from a Supramolecular Coordination Polymer and a Diblock Copolymer. *J. Phys. Chem. B* **2007**, *111*, 11662−11669.

(52) Ding, Y.; Yang, Y.; Yang, L.; Yan, Y.; Huang, J.; Cohen Stuart, M. A. A Case of Adaptive Self-Assembly. *ACS Nano* **2012**, *6*, 1004−1010.

(53) Xu, L.; Feng, L.; Han, Y.; Jing, Y.; Xian, Z.; Liu, Z.; Huang, J.; Yan, Y. Supramolecular Self-Assembly Enhanced Europium(III) Luminescence under Visible Light. *Soft Matter* **2014**, *10*, 4686−4693.

(54) Provencher, S. W. A Constrained Regularization Method for Inverting Data Represented by Linear Algebraic or Integral Equations. *Comput. Phys. Commun.* **1982**, *27*, 213−227.

(55) Provencher, S. W. CONTIN: A General Purpose Constrained Regularization Program for Inverting Noisy Linear Algebraic and Integral Equations. *Comput. Phys. Commun.* **1982**, *27*, 229−242.

(56) Ferrari, M.; Fornasiero, M. C.; Isetta, A. M. MTT Colorimetric Assay for Testing Macrophage Cytotoxic Activity in Vitro. *J. Immunol. Methods* **1990**, *131*, 165−172.